Journal of Wind Engineering and Industrial Aerodynamics, Volume 158, November 2016, Pages 11–25.
DOI:10.1016/j.jweia.2016.09.006

Fluid structure interaction modelling of horizontal-axis wind turbine blades based on CFD and FEA

Lin Wang[1], Robin Quant[1] and Athanasios Kolios[1, *]

[1]Centre for Offshore Renewable Energy Engineering, School of Energy, Environment and Agrifood, Cranfield University, MK43 0AL, UK

Abstract

The increasing size and flexibility of large wind turbine blades introduces considerable aeroelastic effects, which are caused by FSI (fluid structure interaction). These effects might result in aeroelastic instability problems, such as edgewise instability and flutter, which can be devastating to the blades and the wind turbine. Therefore, accurate FSI modelling of wind turbine blades is crucial in the development of large wind turbines. In this study, an FSI model for wind turbine blades at full scale is established. The aerodynamic loads are calculated using a CFD (computational fluid dynamics) model implemented in ANSYS FLUENT, and the blade structural responses are determined using a FEA (finite element analysis) model implemented in ANSYS Static Structural module. The interface of CFD and FEA is based on a one-way coupling, in which aerodynamic loads calculated from CFD modelling are mapped to FEA modelling as load boundary conditions. Validated by a series of benchmark computational tests, the one-way FSI model was applied to the modelling of WindPACT 1.5MW wind turbine blade, a representative large-scale horizontal-axis wind turbine blade. Five operational conditions are assessed, with the worst case found to be near the rated wind speed. Maximum tensile/compressive stresses and tip deflections in each case are found to be within material and structural limits, according to relevant design standards.

[*] Corresponding author. Tel.:+ 44 (0) 1234 754631; E-mail: a.kolios@cranfield.ac.uk

Keywords: wind turbine blade; aeroelasticity; FSI (fluid structure interaction); CFD (computational fluid dynamics); FEA (finite element analysis); WindPACT

1. Introduction

The size of large wind turbines has increased dramatically over the past three decades, from a rated power of 75kW with rotors of 17m diameter for earlier designs up to commercial 5MW turbines with rotors of 125m [1]. However, as a result of growth in size and flexibility of large wind turbine blades, the blades are becoming more susceptible to aeroelastic issues caused by FSI (fluid-structure interaction). Specifically, during the operation of wind turbines, the aerodynamic loads on the blade may cause blade deflection. This deflection can in turn lead to additional variation in the flow field, resulting in further load alteration. The interaction of fluid and structure may lead to aeroelastic instability problems, such as edgewise instability and flutter, which can have a devastating impact on the blade itself and the wind turbine as a system. Therefore, accurate FSI modelling of wind turbine blades is crucial in the development of large wind turbines [2].

FSI modelling requires both aerodynamic and structural components to establish both aerodynamic loads and the corresponding structural responses. Currently, there are a variety of methods for establishing these model components, and approaches for coupling them, in order to investigate FSI behaviour of wind turbine blades.

For the aerodynamic component of FSI modelling, the BEM (blade element momentum) model [3] has been extensively applied due to its efficiency and reasonable accuracy. The high efficiency of the BEM model also makes it suitable for design optimisation, which generally involves a large number of design iterations. Based on the BEM model and different optimisation strategies, a series of case studies has been performed to optimise the aerodynamic performance for both fixed-speed [4, 5] and variable-speed wind turbine blades [6, 7]. However, the BEM model is incapable of providing detailed information on the flow field, such as flow visualisation and wake

development. This information is important for wind turbine designers to have a better understanding of the flow field around the blade and to further optimise the design. Obtaining detailed information on the flow field requires CFD (computational fluid dynamics) modelling [8], which has been receiving greater attention in recent years due to the rapid advancement of computer technology. Compared to BEM model, the CFD model is more computationally expensive, but it is capable of accurately modelling complex 3D (three-dimensional) flow fields and representing realistic fluid dynamics more accurately[9-11]. Due to its high level of accuracy and flexibility, the CFD model is chosen as the aerodynamic component of FSI modelling in this study.

For the structural component of FSI modelling, beam models and FEA (finite element analysis) models are the two most common approaches referred in the literature [12, 13]. Beam models are 1D (one-dimensional) representations of 3D structures which discretise properties such as stiffness and mass into points along the 1D beam. They are computationally efficient and generally give reasonable results. Based on a nonlinear beam model, Wang et al. [14] developed a nonlinear aeroelastic model for wind turbine blades, taking account of both large blade deflections and geometric nonlinearities. The beam model is characterised by cross-sectional properties, such as mass per unit length and cross-sectional stiffness, which can be obtained by using specialised cross-sectional analysis models [15]. However, a beam model is incapable of providing some important information for the blade design, such as detailed stress distributions within the blade structure. In an FEA model, wind turbine composite blades are generally constructed using 3D composite shell elements, which are capable of describing composite layer characteristics throughout the shell thickness. FEA model has the advantages of being high-fidelity and capable of examining the detailed stress distributions within each layer of composite blade structure [16]. For this reason, FEA model is selected as the structural component of FSI modelling in this paper.

The coupling methods for FSI modelling can be roughly categorised into two groups, i.e. two-way coupling and one-way coupling. In a two-way coupling approach, typically the aerodynamic model is solved to acquire load data separately. These loads are then mapped to the structural

model as boundary conditions and used to generate the model deflection. This deflection is then mapped back to the aerodynamic model and the process is repeated until result convergence is achieved. However, whilst full coupling produces the most accurate results through effective model synchronisation, it is computationally expensive due to the frequent transfer of information between models during each time step. In a one-way coupling model, the aerodynamic loads are mapped to the structural model to assess model deflection in the same way as two-way coupling. However, these deflections are not mapped back to the aerodynamic model. Compared to the two-way coupling, the one-way coupling saves much computational resources, making it preferable for initial modelling purposes. Considering the computational efficiency, the one-way coupling is selected as the coupling method of FSI modelling in this study.

Presently, the majority of commercial aeroelastic codes (such as FAST [17], GH-Bladed [18] and HAWC2 [19]) utilise variations of low-order aerodynamic models (e.g. BEM model) to model aerodynamic loading [12, 13]. However, in order to establish complex 3D flow accuracy, higher resolution methods are required.

Studies have been carried out to couple higher resolution methods (such as FEA and CFD) for FSI modelling, and a comprehensive review of aeroelastic modelling of wind turbine blades can be found in Ref. [20]. It should be noted that a wind turbine blade generally has complex structures including several layers of composite materials with shear webs. Due to the difficulties in modelling and analysing a full-scale wind turbine composite blade, majority of FSI modelling have been done on either 2D cross sections of blades or 3D blades with simplified structures. MacPhee and Beyene [21] developed a 2D FSI model to simulate the aeroelastic response of a symmetric NACA 0012 blade subjected to variable loading. Krawczyk et al. [22] developed a similar 2D FSI model based on CFD and FEA and applied it to aeroelastic analysis of a NACA 4412 blade. Bagheri and Nejat [23] developed a 3D FSI model and applied it to aeroelastic analysis of NREL Phase VI rotor. The torque and pressure coefficient at different blade sections over wind speed of 7 to 15 m/s were investigated based on the 3D FSI model. However, the composite blade was simplified by a solid blade (stiffer than the real one) subtracting an inner-

subpart cross section. In order to develop a reliable aeroleastic model of wind turbine composite blades, it is crucial to model the composite blades at full scale and consider the detailed composite layups.

This paper presents a one-way coupled FSI model for wind turbine composite blades at full scale, taking account of detailed composite layups of the blade. The aerodynamic loads are calculated using CFD and blade structural responses are determined using FEA. The coupling strategy is based on the one-way coupling strategy, in which aerodynamic loads calculated from CFD modelling are mapped to FEA modelling as load boundary conditions. The established FSI model is validated by a series of benchmark tests as compared with data reported in the literature, and applied to the FSI simulation of WindPACT 1.5MW horizontal-axis wind turbine [24], which is a representative of megawatt-class horizontal-axis wind turbines. In addition to horizontal axis wind turbines, the established FSI model can be also applied to other similar applications, such as vertical axis wind turbines[25] and tidal devices [26], due to its high flexibility.

This paper is structured as follows. Section 2 presents the methodology comprising four components, i.e. wind turbine model, CFD modelling, FEA modelling and one-way FSI coupling. Results and discussions are presented in Section 3, followed by a conclusion in Section 4.

2. Methods

2.1. Wind turbine model

The wind turbine model used in this study is the WindPACT 1.5MW wind turbine [24, 27-29], which is a reference wind turbine designed by NREL (National Renewable Energy Laboratory) in the WindPACT (Wind Partnership for Advanced Component Technologies) project between years 2000 and 2002. This wind turbine is a conventional three-bladed upwind horizontal-axis wind turbine, utilising variable-speed variable-pitch control. The details of the WindPACT 1.5MW

wind turbine can be found in Refs. [24, 27-29], and its main parameters are summarised in Table 1. The blade includes two shear webs and three types of airfoils, i.e. S818, S825 and S826. The modelled 3D geometry of the blade is presented in Fig. 1.

Table 1. Main parameters of WindPACT 1.5MW wind turbine

Parameters	Values	Units
Rated Power P_{rated}	1.5	MW
Number of blades N_B	3	-
Rotor radius R	35	m
Rated wind speed V_{rated}	11.5	m/s
Rate rotor speed Ω_{rated}	20.5	rpm

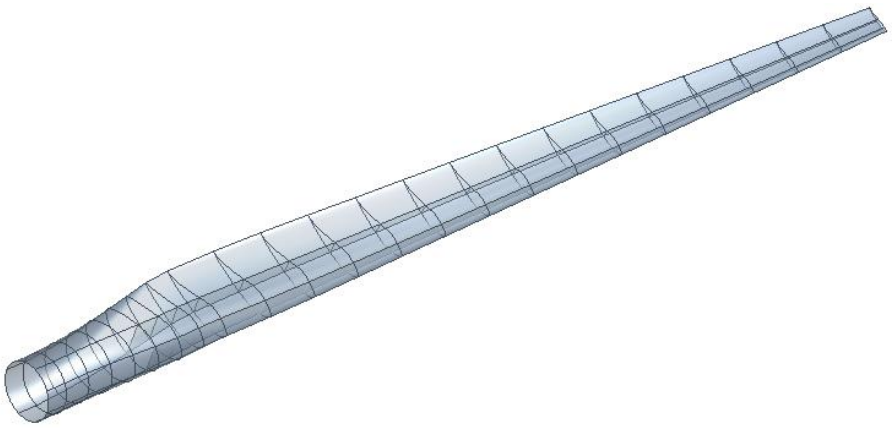

Figure 1. 3D geometry model of WindPACT 1.5MW wind turbine blade

2.2. CFD modelling

A CFD model of wind turbine blades is established using ANSYS FLUENT [30], which is a widely used CFD modelling software. The CFD model is then applied to the CFD modelling of WindPACT 1.5WM wind turbine blades. The computational domain and boundary conditions,

mesh, turbulence model, solution method and convergence criteria used in the CFD modelling are presented in this section.

2.2.1. Computational domain and boundary conditions

As the wind turbine model is symmetrical about its centre of rotation, the three blades can be modelled using a single blade in a 120º radial stream tube domain segment with periodic faces to reduce solution times. The computational domain and boundary conditions for the model are depicted in Fig. 2.

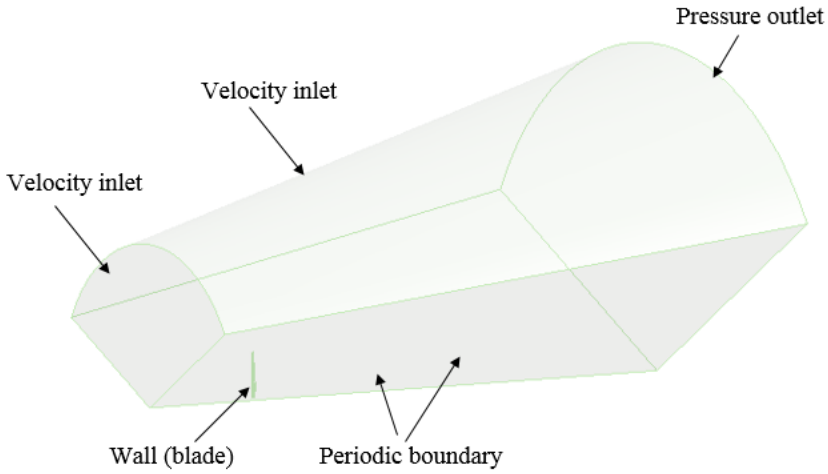

Figure 2. Computational domain and boundary conditions for CFD modelling

The upstream velocity inlet is defined with a 120m radius, offset 90m from the blade and set to the free-stream wind velocity. The pressure outlet is specified at atmospheric pressure and defined with a 240m radius, set back 350m from the turbine blade. The outer surface of the domain is also considered as a velocity inlet with the same velocity as the primary inlet. Further, experiments [31, 32] have shown that wake expansion behind the blade due to the blade rotation is a conical expansion, and therefore the domain in this study uses a conical shape to allow for the wake expansion. The blade is regarded as a stationary non-slip wall, and a rotation frame is applied to the whole computational domain to take account of the rotor rotational speed. This avoids the need for a rotating mesh and allows an inherently unsteady problem to be modelled using a steady-state simulation, significantly reducing computational time.

2.2.2. CFD mesh

Fig. 3 presents the mesh used in the CFD modelling. As can be seen from Fig. 3a, the computational domain is meshed with unstructured mesh. As illustrated in Fig. 3b, prismatic inflation layers are applied to the blade surfaces to have a better resolution of boundary layer flow. Twenty prismatic inflation layers are used, with an expansion rate of 1.35. The first layer height is 4.8e-6m, leading to a small y^+ value (less than 1) around the whole blade surface, as depicted in Fig. 4. y^+ is a non-dimensional wall distance, and it is given by [30]:

$$y^+ = \frac{u_* y}{\nu} \tag{1}$$

where u_* is the friction velocity at the nearest wall, y is the distance to the nearest wall, ν is the local kinematic viscosity of the fluid. In order to ensure accurate modelling of the boundary layer, y^+ value of less than 1 is recommended [12, 30].

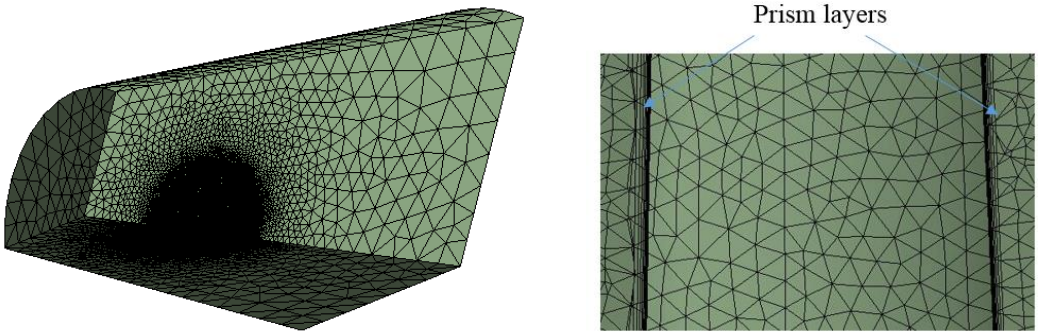

(a) **(b)**

Figure 3. CFD mesh: **a** mesh of the computational domain, **b** prism layers on blade surfaces

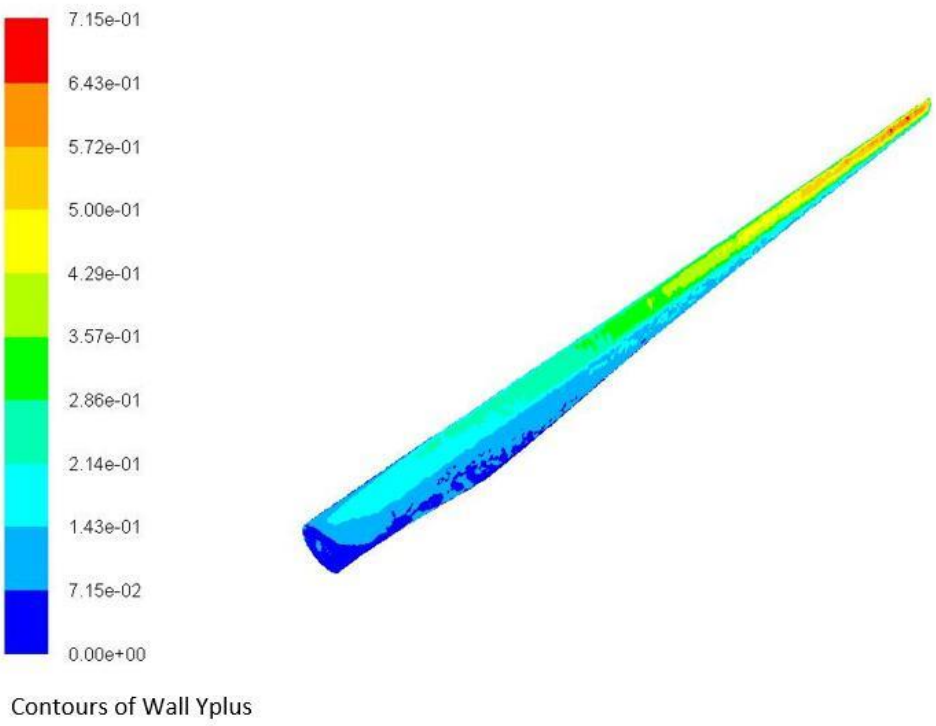

Figure 4. Blade y^+ distribution

In order to determine appropriate cell face size at blade surfaces, a mesh sensitivity study is carried out. In this case, the wind speed, rotor rotational speed and pitch angle are 8m/s, 15rpm and 2.6 degree, respectively. Four cell face size at blade surfaces are investigated, i.e. 0.4m, 0.2m, 0.1m and 0.05m, and the mesh size of the remaining surface is chosen as 1.8m for all cases. The associated total number of elements and the calculated rotor torque are presented in Fig. 5 and Table 2. As can be seen from Fig. 5 and Table 2, the rotor torque converges at a mesh size of 0.1m. Further refining mesh size to 0.05m only obtain 2.51% relative different, but it increase the total number of elements from 2.2 million to 5.5 million, which significantly increases the computational time. Considering computational time and accuracy, the mesh size of 0.1 is deemed as the appropriate cell face size at blade surfaces for CFD modelling in this study.

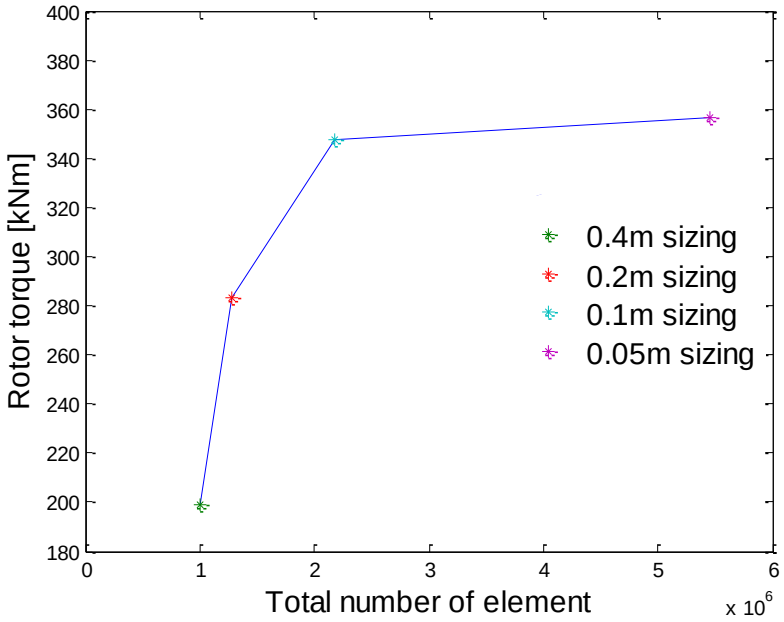

Figure 5. Rotor torque mesh convergence

Table 2. Summary of CFD mesh sensitivity results

Item	Cell face size at blade surfaces			
	0.4m	0.2m	0.1m	0.05m
Rotor torque [Nm]	199,002	283,416	347,490	356,431
Total number of elements	997,219	1,273,460	2,178,899	5,460,679

2.2.3. Turbulence model

The turbulence model used for this study is the $k-\omega$ SST (shear-stress transport) model. This two-equation model developed by Menter [33], has the benefit of being able to switch from a $k-\varepsilon$ turbulence model [34], suited to simulating far field flows, to a $k-\omega$ turbulence model [35], suited to modelling the boundary layer. This model has been used extensively in studies involving wind turbine blades with favourable results [36, 37].

The transport equations for SST model used to calculate the turbulent kinetic energy k and the specific dissipation rate ω can be obtained from Ref. [30].

2.2.4. Solution method

As the problem is in the subsonic region and well below 0.3 Mach, the air can be considered as incompressible [38]. Due to this, the fluid density is approximately constant and has been taken as 1.225kg/m^2. The viscosity is also considered to be constant at 1.7894x10^{-5} kg/ms^{-1}. The incompressible RANS (Reynolds-Averaged Navier-Stokes) equations are solved using the pressure-based coupled algorithm, which solves the momentum and pressure-based continuity equations in a closely coupled manner. Compared to the pressure-based segregated algorithm, in which the momentum and pressure-based continuity equations are solved separately, the pressure-based coupled algorithm significantly improves the convergence rate [30].

2.2.5. Convergence criteria

In order to assess the convergence of the CFD analysis, two criteria are used in this study, i.e. residual values and net mass imbalances.

- Residual values

The residual is one of the mostly used criteria assessing CFD solution convergence. In this study, the residual values of six variables (i.e. continuity, x velocity, y velocity, z velocity, turbulent kinetic energy k and the specific dissipation rate ω) are monitored during the calculation process. The solution is deemed to be converged when these residual values below than 10^{-4} [39, 40], which is the typical value used for residual convergence criterion in the CFD modelling of wind turbine blades. An example of history of residual values is depicted in Fig. 6. In this case, the wind speed, rotor rotational speed, pitch angle are 8m/s, 15rpm, 2.6 degree respectively. As can be seen

from Fig. 6, the residual values of all variables are less than 10^{-4}, meeting the convergence criterion.

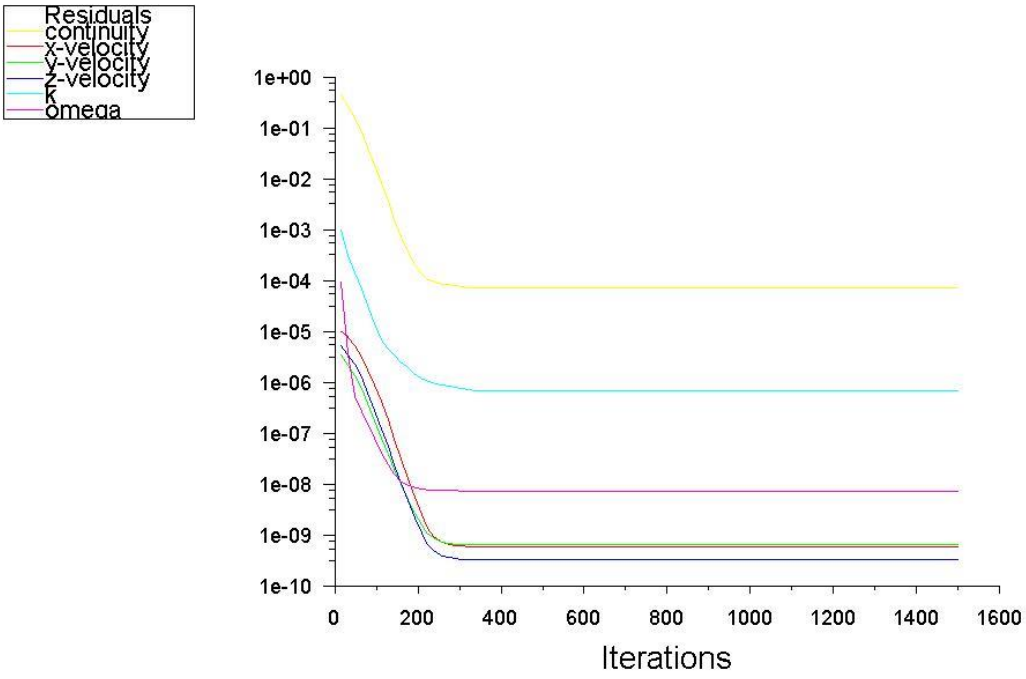

Figure 6. Residuals

- Net mass imbalance

In order to further confirm the convergence, the net mass imbalance is checked. The net mass imbalance of an analysis to be deemed converged should be less than 0.1% [41].

2.2.6. Solve and post-process results

The fluid flow problems involved in this study is highly nonlinear in nature. Therefore, CFD solution must be calculated iteratively. In this study, the number of iteration is set to 1,500, which is a relatively large number ensuring enough iteration to be performed. Additionally, the standard initialisation method is used, and the initial values are computed from inlet boundary.

After the solution is converged, the CFD analysis results, such as aerodynamic pressures and torque acting on the blade can be then plotted using post-processing functions of ANSYS FLUENT.

2.3. FEA modelling

A FEA model of wind turbine composite blades is established using ANSYS Static Structural module [42], which is a widely used FEA modelling software. The FEA model is then applied to the FEA modelling of WindPACT 1.5WM wind turbine blades. The geometry, material properties, composite layups, mesh and boundary conditions used in the FEA modelling are presented in this section.

2.3.1. Geometry

The geometry of the WindPACT 1.5MW wind turbine blade is created based on the aerodynamic shape information (i.e. chord, twist angle and sectional airfoil shape) given in Refs. [24, 27-29]. The created blade geometry is depicted in Fig. 1 of Section 2.1.

2.3.2. Material properties

The WindPACT 1.5MW wind turbine blade is made of five types of materials, i.e. gel coat, random mat, CDB340 triaxial fabric, balsa and spar cap mixture (70% unidirectional and 30% triaxial fabric). A summary of properties of these materials are presented in Table 3.

#

Table 3. Material properties [29]

Material	E_x (GPa)	E_y (GPa)	G_{xy} (GPa)	ν_{xy}	ρ (kg/m^3)
Gel coat	3.44	3.44	1.38	0.3	1230
Random mat	9.65	9.65	3.86	0.3	1670
CDB340 triaxial fabric	24.2	8.97	4.97	0.39	1700
Balsa	2.07	2.07	0.14	0.22	144
Spar cap mixture	27.1	8.35	4.7	0.37	1700

(where E_x is the longitudinal Young's modulus; E_y is the lateral Young's modulus; G_{xy} is the shear modulus; ν_{xy} is the Poisson's ratio; ρ is the material density)

2.3.3. Composite layups

The schematic of the blade structure is depicted in Fig. 7.

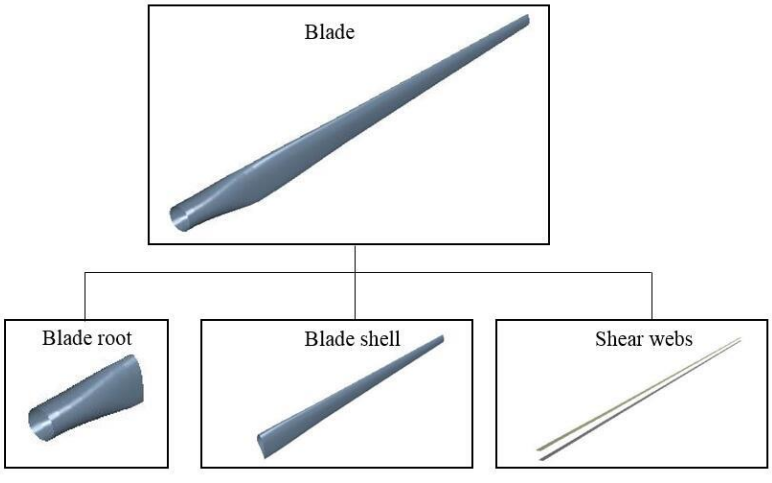

Figure 7. Schematic of blade structure

As can be seen from Fig. 7, the blade structure consists of three part, i.e. blade root, blade shell and shear webs, of which composite stacks are presented below.

- **Blade root**

The blade root does not include a balsa core and is mainly constituted of a spar cap mixture. The composite stacks of the blade root are presented in Table 4.

Table 4. Composite stacks of blade root [29]

Layer	Material	Thickness [mm]
1	Gel coat	0.51
2	Random mat	0.38
3	Triaxial fabric	0.89
4	Spar cap mixture	15.0
5	Triaxial fabric	0.89

- **Blade shell**

Composite layups of the blade shell have a core thickness that is defined as a function of blade geometry, i.e. chord length c or airfoil thickness t. Table 5 presents the composite layups of blade shell.

Table 5. Composite layups of blade shell [29]

Layer	Material	Thickness [mm]
1	Gel coat	0.51
2	Random mat	0.38
3	Triaxial fabric	0.89
4		
0% - 15% c	Balsa	0.5% c
15% - 50% c	Spar cap mixture	specified % t/c
50% - 85% c	Balsa	1.0% c
5	Triaxial fabric	0.89

In Table 5, the specified % t/c for the spar cap mixture transitions from 8.3 at 25% blade span to 6.5 at 75% blade span.

- **Shear webs**

The shear webs consist of triaxial fabric and balsa. Table 6 presents the composite layups of the shear webs.

Table 6. Composite stacks of shear webs [29]

Layer	Material	Thickness [mm]
1	Triaxial fabric	0.89
2	Balsa	1.0% c
3	Triaxial fabric	0.89

2.3.4. FEA mesh

The blade structure is meshed using structured mesh with shell elements. In order to determine appropriate mesh size, a mesh sensitivity exercise is carried out, considering four mesh sizes, i.e. 0.4m, 0.2m, 0.1m and 0.05m. In this exercise, the blade is non-rotating, and a fixed boundary condition is applied to the blade root. The first 6 modal frequencies of the blade are evaluated, and the analysis results are presented in Table 7. As can be seen from Table 7, the modal frequencies converge at a mesh size of 0.1m, with a maximum relative difference (0.047%) occurring for the 1st edgewise mode when compared to further mesh refinement with a mesh size of 0.05m. Therefore, 0.1m is deemed as the appropriate mesh size. The created mesh is depicted in Fig. 8a, and a close view of the blade tip is presented in Fig. 8b.

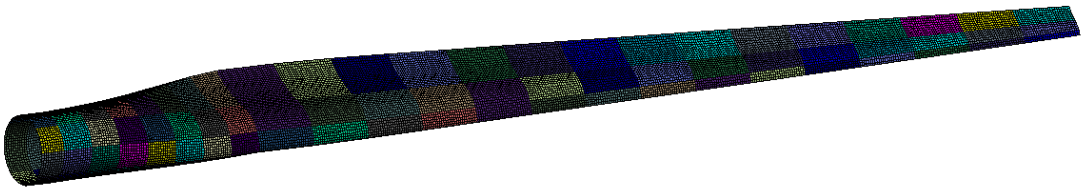

(a)

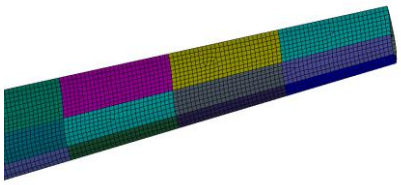

(b)

Figure 8. FEA Mesh: **a** blade, **b** close view of blade tip

Table 7. FEA mesh sensitivity analysis

ID	Mode frequencies	0.4m sizing	0.2m sizing	0.1m sizing	0.05m sizing	Diff (%)
1	1st flapwise (Hz)	1.0411	1.0555	1.0508	1.0512	0.038
2	1st edgewise (Hz)	1.7081	1.7030	1.7003	1.7011	0.047
3	2nd flapwise (Hz)	2.8747	2.9303	2.9329	2.9336	0.024
4	2nd edgewise (Hz)	5.0439	4.9846	4.9672	4.9685	0.026
5	3rd flapwise (Hz)	6.2477	6.3835	6.3978	6.3985	0.011
6	4th flapwise (Hz)	9.9076	10.000	10.034	10.038	0.040

(Notes: diff (%) column presents the relative difference of 0.1m sizing with respect to 0.05m sizing)

2.3.5. Boundary conditions

In addition to aerodynamic loads, there are two other important sources of loads on the blades, i.e. 1) gravity loads, which are introduced by the gravity acting on the blades; and 2) centrifugal loads, which are caused by the rotation of the blades. In this study, the rotor rotational speed is applied to

the blade structure to take account of the centrifugal loads, and the gravity loads are also applied to the blade structure as a static load. Additionally, a fixed boundary condition is applied to the blade root.

2.3.6. Solve and post-process results

Having defined blade geometry, material properties, composite layups, mesh and boundary conditions, different types of structural analysis, such as static analysis and modal analysis can be performed. The analysis results, such as blade deformations, stress distributions and modal shapes can be then plotted using post-processing functions of ANSYS software.

2.4. One-way FSI coupling

The coupling method of the FSI modelling is based on the one-way coupling. The fluid field is solved using CFD until the convergence criteria are reached. The aerodynamic pressures on the blade obtained from CFD modelling are then mapped to the FEA model as load boundary conditions. After that, the FEA model is use to calculated the structural responses of the blade (such as deformation and stress distributions) subjected to aerodynamic, gravity and centrifugal loads. The schematic of the one-way FSI modelling is presented in Fig. 9. The details of CFD and FEA in the FSI model are presented previously in Sections 2.2 and 2.3, respectively.

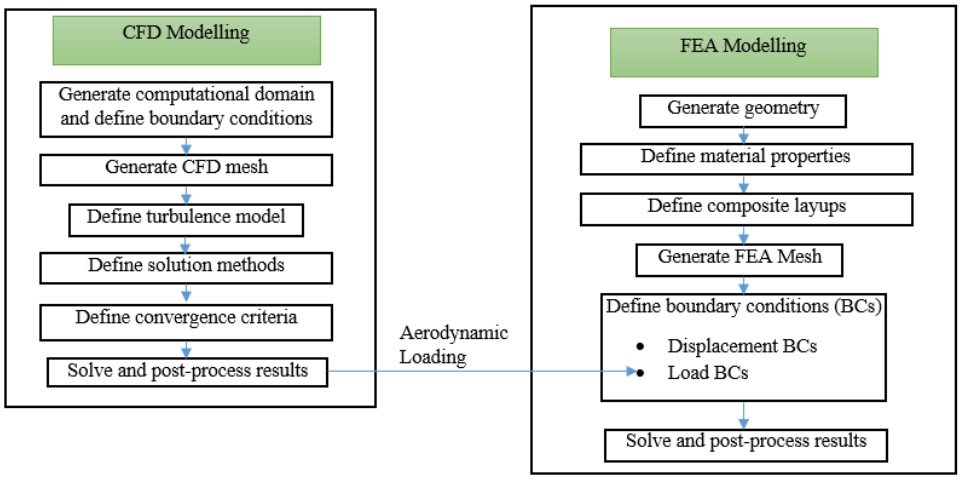

Figure 9. Schematic of one-way FSI modelling

3. Results and discussions

Based on the method presented in Section 2, a one-way FSI model for horizontal-axis wind turbine blades is established and validated by a series of benchmark calculation tests. The components of the one-way FSI model, i.e. the aerodynamic component based on CFD and the structural component based on FEA, are validated independently. After the validation, the FSI model is applied to the FSI modelling of the WindPACT 1.5MW wind turbine blade to examine its pressure distributions, deflections and stress distributions.

3.1. Comparison with established models

The validation of the FSI model comprises two parts: 1) validation of its aerodynamic component against available power curve data reported in the literature; and 2) validation of its structural component against modal analysis results reported in the literature.

3.1.1. Validation of CFD model

In order to validate the CFD model presented in Section 2.2, two case studies are performed. In the first case study, the power curve from the CFD model is compared with the results from NREL FAST code [17]. In the second case study, the blade pressure coefficients C_p from the CFD model are compared with the results from inviscid model.

3.1.1.1. Comparison with NREL FAST code

This case study aims to validate the CFD model presented in Section 2.2 against FAST code [17], in which aerodynamic loads are calculated based on BEM (blade element momentum) model. FAST code has been developed by NREL (National Renewable Energy Laboratory) to model both two- and three-bladed horizontal-axis wind turbines, and it has been widely used in wind turbine

research organisations and industrial practices. In 2005, GL (Germanisher Lloyd), one of the leading certification organisations in wind energy field, issued FAST a certification on its load calculation of onshore wind turbines [17]. In this study, the WindPACT 1.5MW wind turbine blade is simulated at five different operational conditions, of which free-stream wind speed, rotor rotational speed and blade pitch angle are presented in Fig.10 and Table 8.

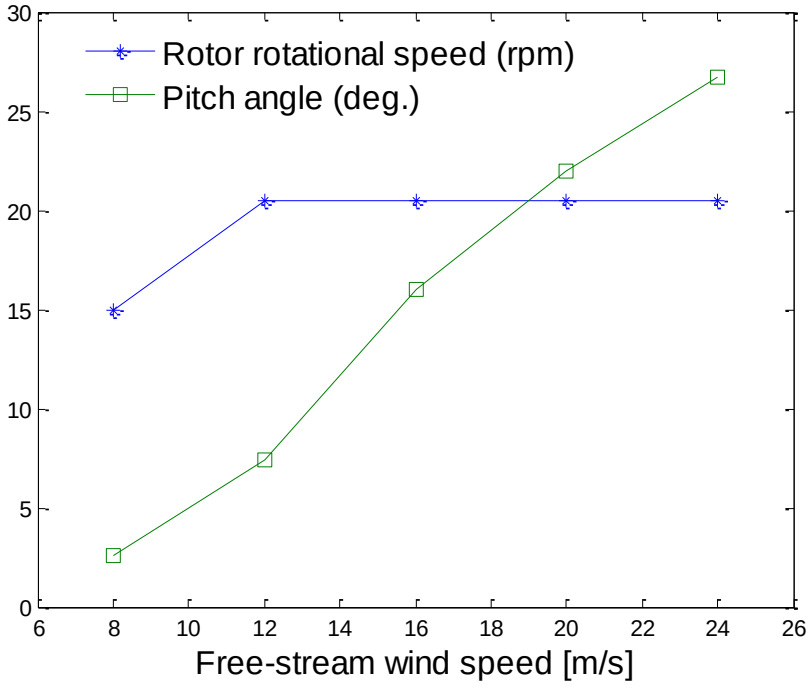

Figure 10. Operational conditions

Table 8. Operational conditions

Operational condition ID	Free-stream wind speed [m/s]	Rotor rotational speed [rpm]	Blade pitch angle [deg.]
1	8	15.0	2.6
2	12	20.5	7.4
3	16	20.5	16.0
4	20	20.5	22.0
5	24	20.5	26.7

The CFD model presented in Section 2.2 is used to calculate the torque of the WindPACT 1.5MW wind turbine rotor under the above five operational conditions. After obtaining the rotor torque T, the generator power P_G can be easily determined using the following equation:

$$P_G = \Omega T \eta \tag{4}$$

where Ω is the rotor rotational speed; η is the drivetrain efficiency with a value of 0.925 given in Ref. [27].

Fig. 11 presents the comparison of the results calculated from the CFD model and the FAST code results reported in Ref. [43].

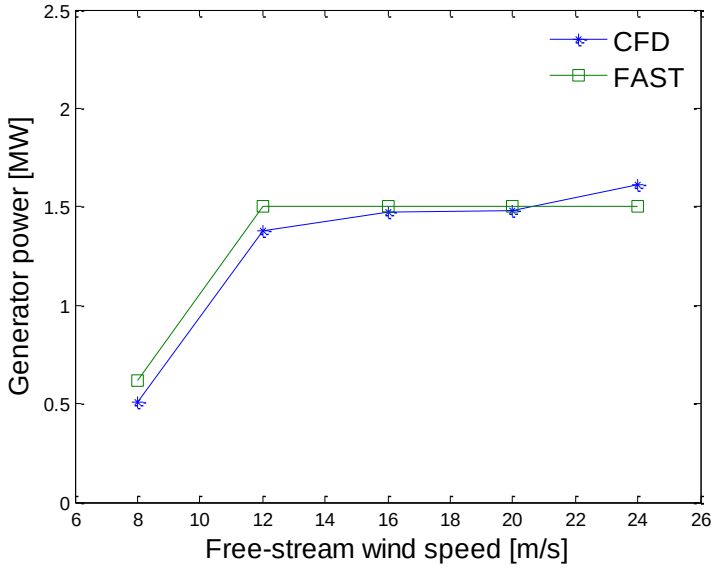

Figure 11. Generator power of WindPACT 1.5MW wind turbine

As can be seen from Fig. 11, the results from the CFD model show reasonable agreement with the results from FAST code, with maximum percentage difference (18.6%) occurring at wind speed of 8m/s. This confirms the validity of the CFD model.

3.1.1.2. Comparison with inviscid model

For each operational condition presented in Table 8, the non-dimensional pressure coefficient C_p is taken at two spanwise sections (i.e. $0.75R$ and $0.971R$), corresponding to airfoil profiles S825 and S826. C_p plots obtained from CFD are compared to the inviscid pressure distributions for each airfoil at the sectional angle of attack reported in a NREL report [44]. The comparison results are presented in Figs. 12 to 16.

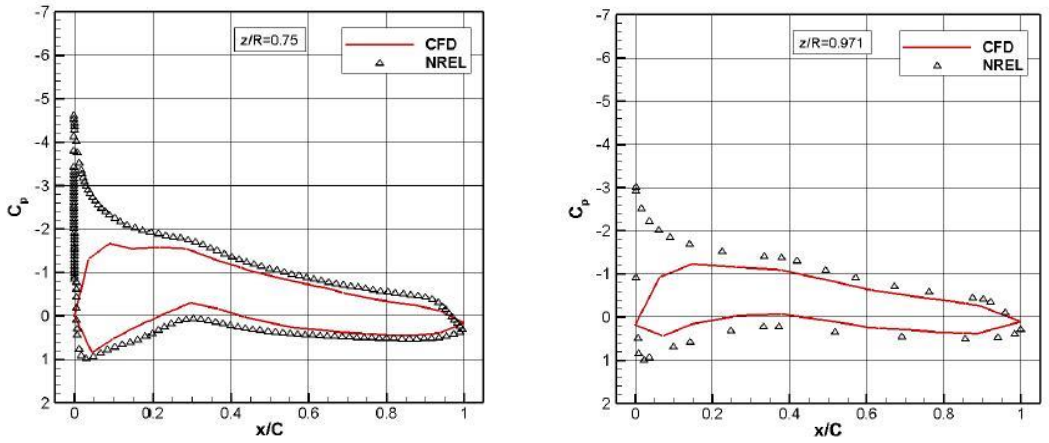

(a) **(b)**

Figure 12. 8m/s case C_p contours: **a** S825 at $\alpha = 8°$, **b** S826 $\alpha = 6°$

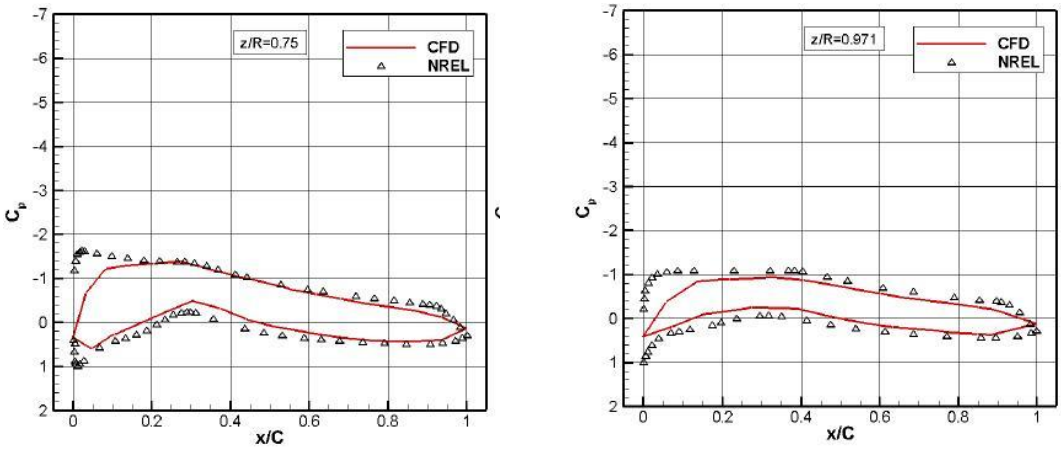

(a) **(b)**

Figure 13. 12m/s case C_p contours: **a** S825 at $\alpha = 4°$, **b** S826 at $\alpha = 2°$

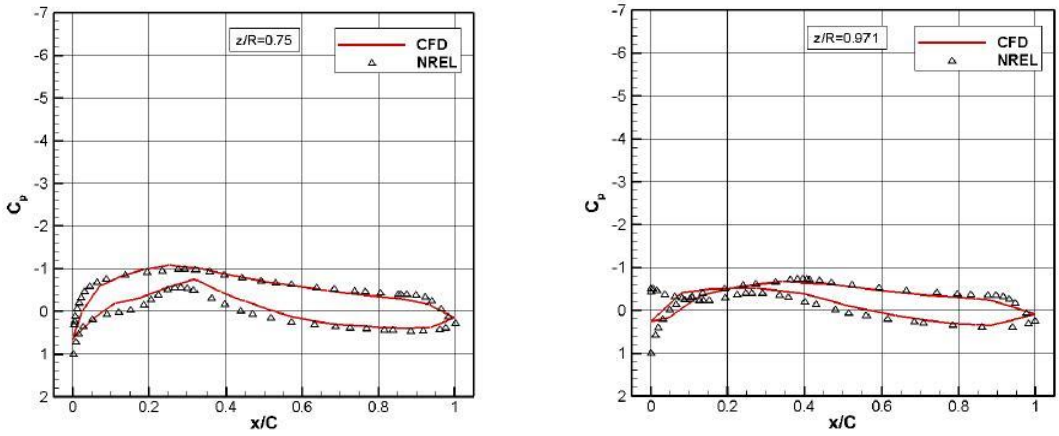

449

450 **(a)** **(b)**

451 Figure 14. 16m/s case C_p contours: **a** S825 at $\alpha = 0°$, **b** S826 at $\alpha = -3°$

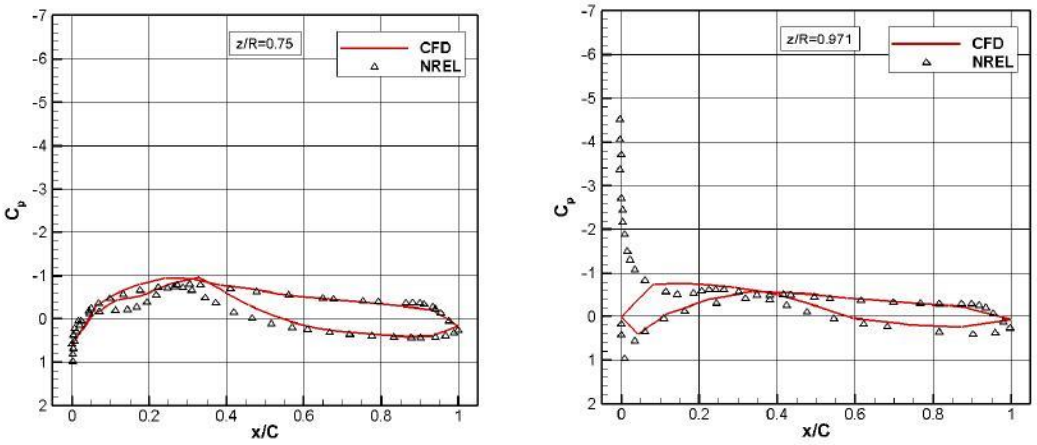

452

453 **(a)** **(b)**

454 Figure 15. 20m/s case C_p contours: **a** S825 at $\alpha = -2°$, **b** S826 at $\alpha = -6°$

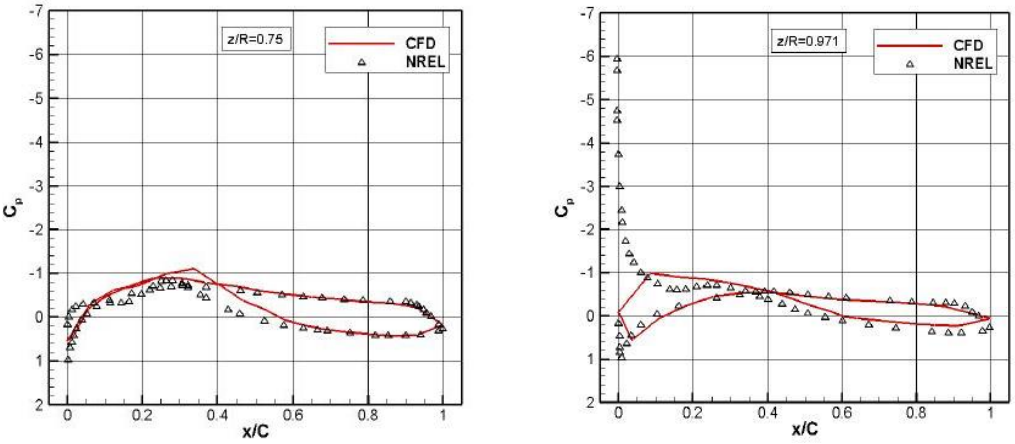

455

456 **(a)** **(b)**

457 Figure 16. 24m/s case C_p contours: **a** S825 at $\alpha = -4°$, **b** S826 at $\alpha = -7°$

As can be seen from Figs. 12 to 16, the results from CFD shown reasonable agreement with the results from inviscid model, both in terms of distribution shape and C_p magnitude. It should also be noted that, compared to CFD model, over predictions of leading edge pressure peaks are observed in inviscid model. This is caused by the use of potential theory in inviscid model. Specifically, as viscous effects are not considered in potential theory, the fluid accelerates away from leading edge stagnation points at a greater rate than in reality, due to a lack of viscous-induced aerodynamic drag. This over predictions of leading edge pressure peaks in inviscid model has been shown to occur in other studies when comparing potential flow theory to experimental data [45, 46]. Additionally, the sectional angles of attack are calculated using NREL FAST code under the same flow condition with the CFD model, but the calculated values have been rounded because the inviscid plots are only available at fixed integer values. This may also lead to discrepancies between the inviscid plots and CFD results.

3.1.2. Validation of FEA model

This case study aims to validate the FEA model presented in Section 2.3 against modal frequencies provided in the Sandia NuMAD Blade Model Report [29]. The FEA model presented in Section 2.3 is used to perform the modal analysis of the WindPACT 1.5MW wind turbine blade. In this case, the blade is non-rotating and free-vibration (no loads on the blade). A fixed boundary condition is applied to the blade root. The first six blade modal shapes (including four flapwise modes and two edgewise modes) obtained from the FEA model are depicted in Figs. 17 and 18.

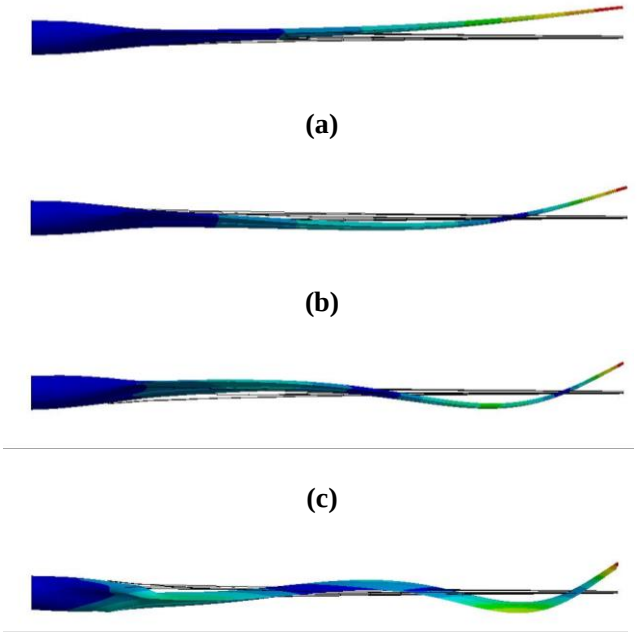

(a)

(b)

(c)

(d)

Figure 17. Modal shapes of blade flapwise modes: **a** 1st, **b** 2nd, **c** 3rd, **d** 4th

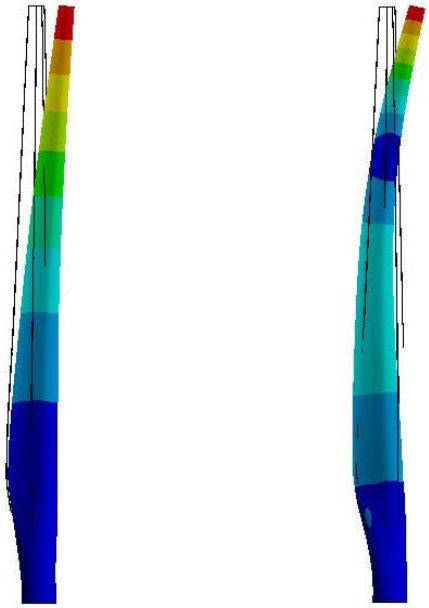

(a) **(b)**

Figure 18. Modal shapes of blade edgewise modes: **a** 1st, **b** 2nd

The modal frequency results from the present FEA model are compared against the FEA results reported in the Sandia NuMAD Blade Model Report [29], as shown in Fig. 19.

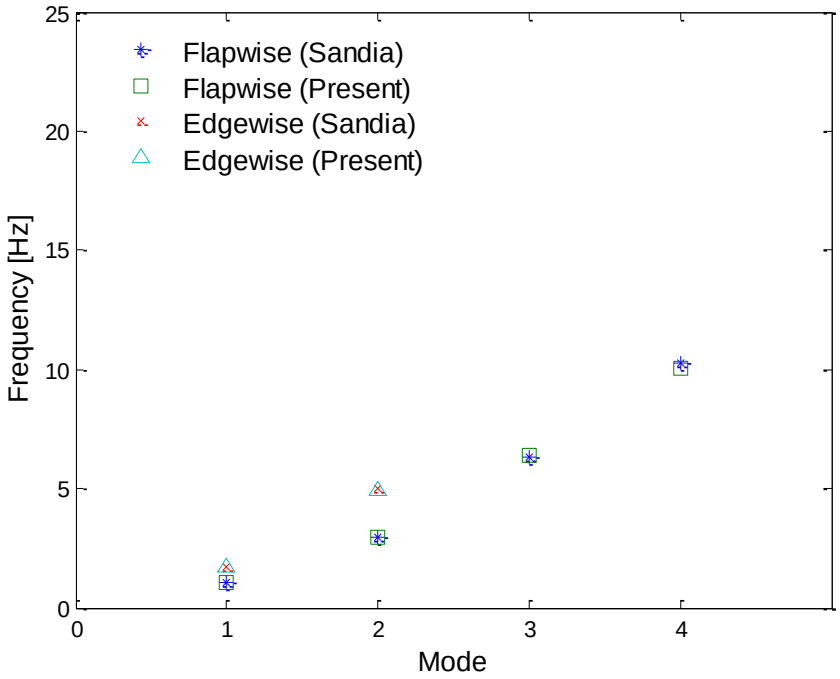

Figure 19. Mode frequencies of WindPACT 1.5MW wind turbine blade

As can be seen from Fig. 19, the flapwise and edgewise blade mode frequencies calculated from the present FEA model match well with the FEA results reported in Ref. [29], with maximum percentage difference (2.6%) observing at the 4th flapwise mode. This confirms the validity of the present FEA model.

3.2. FSI modelling results

Based on the one-way FSI model, the pressure distributions, deflections and stress distributions of the WindPACT 1.5MW wind turbine blade under five operational conditions (see Table 8) are examined.

3.2.1. Pressure distributions

For each operational condition (see Table 8), pressure contours on both blade front (pressure) and back (suction) sides are produced, as shown in Fig.20.

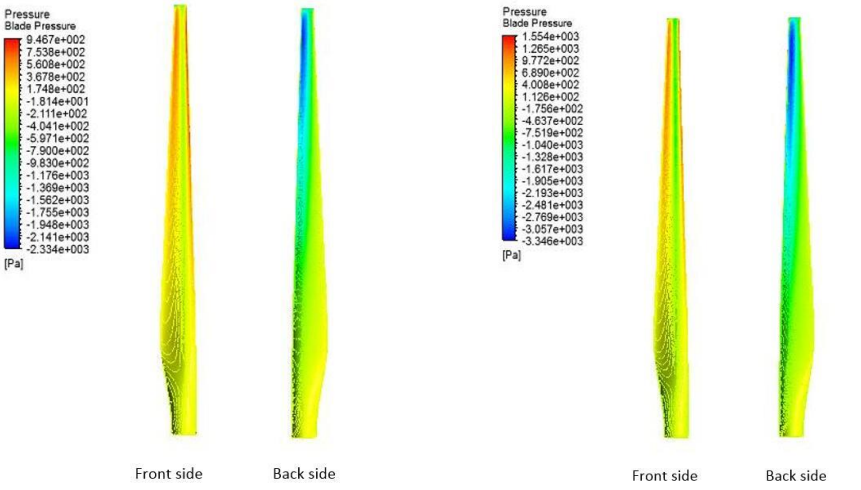

519

520 **(a)** **(b)**

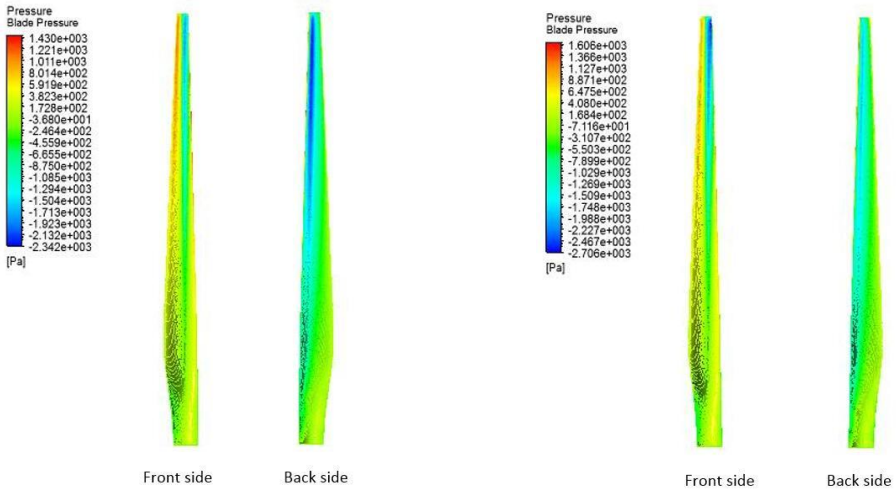

521

522 **(c)** **(d)**

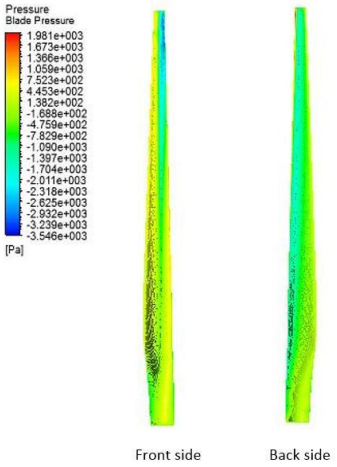

523

524 **(e)**

525 Figure 20. Blade pressure distributions: **a** 8m/s case, **b** 12m/s case, **c** 16m/s case, **d** 20m/s case, **e**

526 24m/s

Initially, as can be seen from Figs. 20a and 20b, the highest negative pressures are observed on the leading edge of blade suction surface, and the highest positive pressures occur near the leading edge of blade pressure surface. However, as the blade is pitched towards feathering, the blade becomes more parallel (collinear) with the airflow. This causes the stagnation points to be shifted onto the suction surface, resulting in lower negative pressures on the rear of the blade due to reduced air velocity. The pitching action also results in faster moving airflow over the underside of the blade, leading to suction on the pressure surface. This results in a pressure sign reversal between the two surfaces.

3.2.2. Deflections

The blade total deformations under five operational conditions are depicted in Fig. 21.

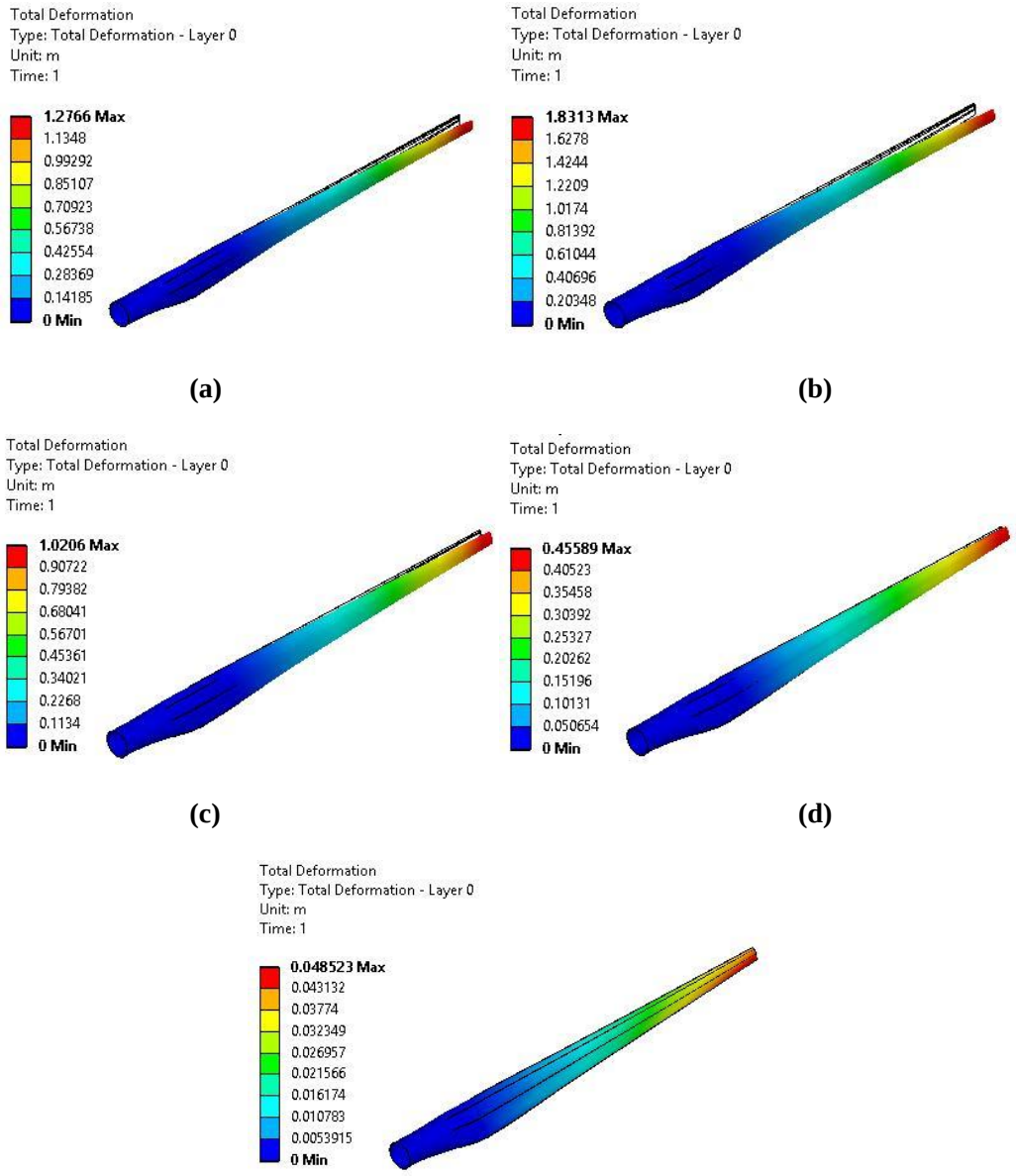

Figure 21. Blade total deformations: **a** 8m/s case, **b** 12m/s case, **c** 16m/s case, **d** 20m/s case, **e** 24m/s case

As can be seen from Fig. 21, for all operational conditions, the maximum deformation occurs on the blade tip. The blade-tip flapwise and edgewise deflections under five operational conditions are presented in Fig. 22.

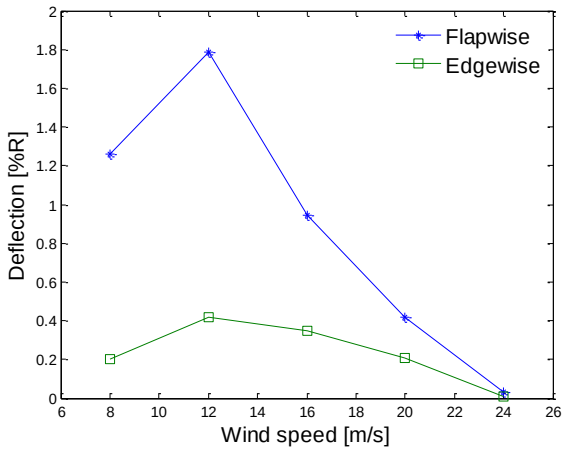

Figure 22. Blade-tip flapwise and edgewise deflections

As can be seen from Fig. 22, the blade-tip deflection increases as the wind speed approaches 12m/s. However, as the blade is increasingly pitched towards feathering above the wind speed of 12m/s, the blade-tip deflection decreases. This increasing-decreasing deflection behaviour is supported by the pressure distributions shown in Fig. 20, as pressures at blade pressure side are seen to first increase from 8 to 12m/s and then blade pressures become increasing more balanced on upper and lower surfaces from 12 to 24m/s as the blade is pitched. It is therefore intuitive that this would result in increasing-decreasing deflection as shown in Fig. 22.

Additionally, the turbine hub is specified with an overhang (tower clearance) of 3.3m. The maximum blade-tip flapwise deflection 1.785m (observed at wind speed of 12m/s) is much lower than this value, indicating the blade is not likely to strike on the tower under the given five operational conditions.

3.2.3. Stress distributions

All five operational conditions are considered for the blade stress analysis. Both compressive and tensile stresses are examined in the triaxial fabric, the third layer of the composite blade. A comparison of maximum compressive and tensile stresses in this material for five cases are shown in Table 9. As can be seen from Table 9, both maximum tensile and compressive stresses occur at

wind speed of 12m/s, corresponding to maximum blade-tip flapwise deflection. The stress distributions of the blade for five cases are presented in Fig. 23. As can be seen from Fig. 23, the majority of maximum stresses are found to occur in the blade root region, primarily at its junction between the shear webs. However, for the 24m/s case (see Fig. 23e), due to a reduced root bending moment, the maximum tensile and compressive stresses are identified at the blade suction surface, in leading edge panels 21m and 22.75m from the root, respectively.

Table **9.** Triaxial fabric peak stress comparison

U_∞ (m/s)	Material	Layer	Max Tensile Stress (Pa)	Max Compressive Stress (Pa)
8	Triaxial fabric	3	5.66E+07	-5.64E+07
12	Triaxial fabric	3	8.25E+07	-8.30E+07
16	Triaxial fabric	3	5.12E+07	-5.12E+07
20	Triaxial fabric	3	3.51E+07	-3.42E+07
24	Triaxial fabric	3	1.76E+07	-2.14E+07

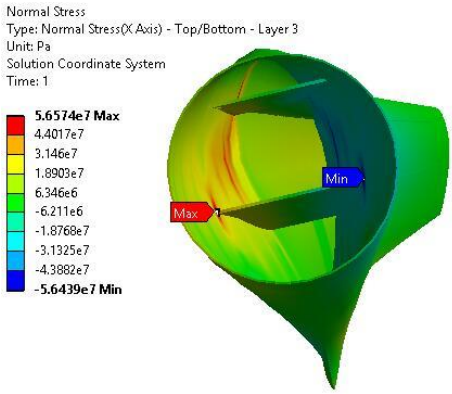

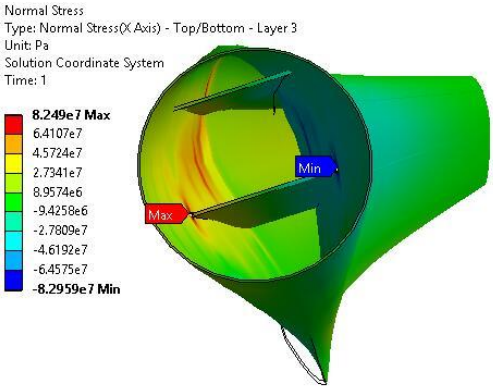

(a) **(b)**

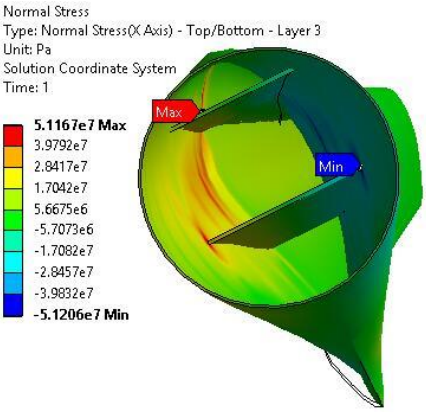

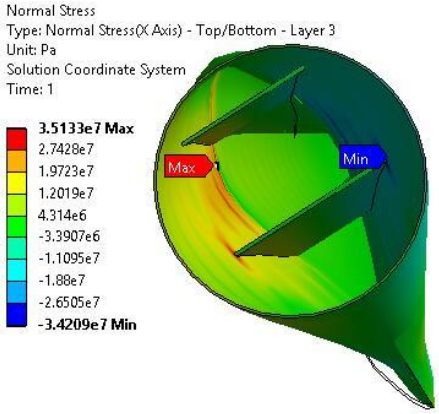

(c) **(d)**

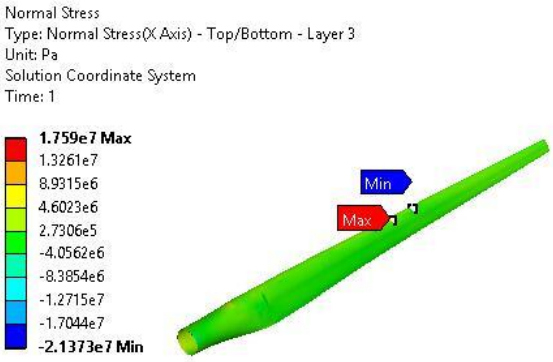

(e)

Figure 23. Normal stress distributions: **a** 8m/s case, **b** 12m/s case, **c** 16m/s case, **d** 20m/s case, **e** 24m/s case

Under the worst case with wind speed 12m/s, the maximum tensile stress (positive normal stress) and maximum compressive stress (negative normal stress) are respectively found to be 82.5MPa and 83.0MPa, which are well below the triaxial fabric's maximum tensile and compressive

strength (typically in the order to 200-300MPa [47]). According to GL design standard [48] and Refs. [49, 50], the material safety factor for wind turbine composite blades is 2.204. In this case study, the minimum material safety factor is about 2.4, which is higher than 2.204. This indicates the blade is unlikely to experience material failure under the given five operational conditions.

4. Conclusion

In this study, a FSI (fluid structure interaction) model for horizontal-axis wind turbine blades has been established by coupling CFD (computational fluid dynamics) and FEA (finite element analysis). The coupling strategy is based on one-way coupling, in which the aerodynamic loads calculated by CFD modelling are mapped to FEA modelling as load boundary conditions. Validated by a series of benchmark computational tests, the FSI model was applied to the FSI modelling of WindPACT 1.5MW wind turbine blade, a representative of large-scale horizontal-axis wind turbine blades. The following conclusions can be drawn from the present study:

1) Reasonable agreement (with maximum percentage difference of 18.6%) is achieved in comparison with FAST code, which confirms the validity of the aerodynamic component (based on CFD) of the FSI model.

2) Good agreement (with maximum percentage difference of 2.6%) is achieved in comparison with the modal frequencies provided in the Sandia NuMAD Blade Mode Report, which confirms the validity of the structural component (based on FEA) of the FSI model.

3) Based on the FSI model, the blade pressure distributions, deflections and stress distributions are examined under five operational conditions (wind speed 8m/s, 12m/s, 16m/s, 20m/s and 24m/s).

4) The blade pressure coefficients C_p from the present model show reasonable agreement with the results from inviscid model, both in terms of distribution shape and magnitude.

5) The maximum blade-tip flapwise deflection (1.785m) is observed at 12m/s wind speed case, which is lower than the tower clearance (3.3m), indicating the blade is not likely to strike on the tower under the given five operational conditions.

6) The maximum tensile stress and maximum compressive stress at the third layer of composite blade are respectively found to be 82.5MPa and 83.0MPa, which are well below the material strength limits, indicating the blade is unlikely to experience material failure under the given five operational conditions.

Additionally, the established one-way FSI model can be also applied to other similar applications, such as vertical axis wind turbines and tidal devices, due to its high flexibility.

References

[1] M. Premalatha, T. Abbasi, and S. Abbasi, "Wind energy: Increasing deployment, rising environmental concerns," *Renewable and Sustainable Energy Reviews,* vol. 31, pp. 270-288, 2014.

[2] L. Wang, "Nonlinear aeroelastic modelling of large wind turbine composite blades," University of Central Lancashire, 2015.

[3] H. Glauert, "Airplane propellers," *Aerodynamic theory,* vol. 4, pp. 169-360, 1935.

[4] L. Wang, X. Tang, and X. Liu, "Blade Design Optimisation for Fixed-Pitch Fixed-Speed Wind Turbines," *ISRN Renewable Energy,* 2012.

[5] X. Liu, L. Wang, and X. Tang, "Optimized linearization of chord and twist angle profiles for fixed-pitch fixed-speed wind turbine blades," *Renewable Energy,* vol. 57, pp. 111-119, 2013.

[6] L. Wang, X. Tang, and X. Liu, "Optimized chord and twist angle distributions of wind turbine blade considering Reynolds number effects," presented at the WEMEP, India, 2012.

[7] J. Zhao, X. W. Liu, L. Wang, and X. Z. Tang, "Design attack angle analysis for fixed-pitch variable-speed wind turbine," *Advanced Materials Research,* vol. 512, pp. 608-612, 2012.

[8] J. Tu, G. H. Yeoh, and C. Liu, *Computational fluid dynamics: a practical approach*: Butterworth-Heinemann, 2012.

[9] B. Plaza, R. Bardera, and S. Visiedo, "Comparison of BEM and CFD results for MEXICO rotor aerodynamics," *Journal of Wind Engineering & Industrial Aerodynamics,* vol. 145, pp. 115-122, 2015.

[10] A. Orlandi, M. Collu, S. Zanforlin, and A. Shires, "3D URANS analysis of a vertical axis wind turbine in skewed flows," *Journal of Wind Engineering & Industrial Aerodynamics,* vol. 147, pp. 77-84, 2015.

[11] A. Makridis and J. Chick, "Validation of a CFD model of wind turbine wakes with terrain effects," *Journal of Wind Engineering & Industrial Aerodynamics,* vol. 123, pp. 12-29, 2013.

[12] M. O. L. Hansen, J. N. Sørensen, S. Voutsinas, N. Sørensen, and H. A. Madsen, "State of the art in wind turbine aerodynamics and aeroelasticity," *Progress in aerospace sciences,* vol. 42, pp. 285-330, 2006.

[13] P. Zhang and S. Huang, "Review of aeroelasticity for wind turbine: Current status, research focus and future perspectives," *Frontiers in Energy,* vol. 5, pp. 419-434, 2011.

[14] L. Wang, X. Liu, N. Renevier, M. Stables, and G. M. Hall, "Nonlinear aeroelastic modelling for wind turbine blades based on blade element momentum theory and geometrically exact beam theory," *Energy,* vol. 76, pp. 487-501, 2014.

[15] L. Wang, X. Liu, L. Guo, N. Renevier, and M. Stables, "A mathematical model for calculating cross-sectional properties of modern wind turbine composite blades," *Renewable Energy,* vol. 64, pp. 52-60, 2014.

[16] L. Wang, A. Kolios, T. Nishino, P.-L. Delafin, and T. Bird, "Structural optimisation of vertical-axis wind turbine composite blades based on finite element analysis and genetic algorithm," *Composite Structures,* 2016.

[17] J. M. Jonkman and M. L. Buhl Jr, "FAST user's guide," *Golden, CO: National Renewable Energy Laboratory*, 2005.
[18] E. Bossanyi, "GH Bladed user manual," *Garrad Hassan and Partners Ltd*, 2009.
[19] T. Larsen, "How 2 HAWC2, the user's manual," *RisøReport, Risø*, 2009.
[20] L. Wang, X. Liu, and A. Kolios, "State of the art in the aeroelasticity of wind turbine blades: Aeroelastic modelling," *Renewable and Sustainable Energy Reviews*, vol. 64, pp. 195-210, 2016.
[21] D. MacPhee and A. Beyene, "Fluid-structure interaction of a morphing symmetrical wind turbine blade subjected to variable load," *International Journal of Energy Research*, vol. 37, pp. 69-79, 2013.
[22] P. Krawczyk, A. Beyene, and D. MacPhee, "Fluid structure interaction of a morphed wind turbine blade," *International Journal of Energy Research*, vol. 37, pp. 1784-1793, 2013.
[23] E. Bagheri and A. Nejat, "Numerical aeroelastic analysis of wind turbine NREL Phase VI Rotor," *Energy Equipment and Systems*, vol. 3, pp. 45-55, 2015.
[24] D. Malcolm and A. Hansen, "WindPACT turbine rotor design study," *National Renewable Energy Laboratory, Golden, CO*, vol. 5, 2002.
[25] A. Kolios, A. Chahardehi, and F. Brennan, "Experimental determination of the overturning moment and net lateral force generated by a novel vertical axis wind turbine: experiment design under load uncertainty," *Experimental Techniques*, vol. 37, pp. 7-14, 2013.
[26] M. Pintar and A. J. Kolios, "Design of a Novel Experimental Facility for Testing of Tidal Arrays," *Energies*, vol. 6, pp. 4117-4133, 2013.
[27] D. A. Griffin, "WindPACT Turbine design scaling studies technical area 1œComposite blades for 80-to 120-meter rotor," *National Renewable Energy Laboratory Technical report*, 2001.
[28] D. Malcolm and A. Hansen, "WindPACT turbine rotor design, specific rating study," *National Renewable Energy Laboratory, Golden, CO*, 2003.
[29] B. Resor and T. Bushnell, "A 1.5 MW NuMAD Blade Model," *Draft Report, Sandia National Laboratories, Albuquerque, NM*, 2011.
[30] A. Fluent, "Ansys fluent 15.0 theory guide," *Ansys Inc*, 2013.
[31] M. M. Hand, D. Simms, L. Fingersh, D. Jager, J. Cotrell, S. Schreck, *et al.*, *Unsteady aerodynamics experiment phase VI: wind tunnel test configurations and available data campaigns*: National Renewable Energy Laboratory Golden, Colorado, USA, 2001.
[32] *http://www.arising.com.au/aviation/windturbines/wind-turbine.html; accessed on 01-06-2016.*
[33] F. R. Menter, "Zonal two equation k-turbulence models for aerodynamic flows," *AIAA paper*, vol. 2906, p. 1993, 1993.
[34] W. Jones and B. Launder, "The prediction of laminarization with a two-equation model of turbulence," *International journal of heat and mass transfer*, vol. 15, pp. 301-314, 1972.
[35] D. Wilcox and F. by Institutions, "Formulation of the k-omega Turbulence Model Revisited."
[36] N. N. Sørensen, J. Michelsen, and S. Schreck, "Navier–Stokes predictions of the NREL phase VI rotor in the NASA Ames 80 ft× 120 ft wind tunnel," *Wind Energy*, vol. 5, pp. 151-169, 2002.
[37] J.-O. Mo and Y.-H. Lee, "CFD Investigation on the aerodynamic characteristics of a small-sized wind turbine of NREL PHASE VI operating with a stall-regulated method," *Journal of mechanical science and technology*, vol. 26, pp. 81-92, 2012.
[38] J. D. Anderson Jr, *Fundamentals of aerodynamics*. New York: Tata McGraw-Hill Education, 2011.
[39] M. M. Yelmule and E. A. Vsj, "CFD predictions of NREL phase VI rotor experiments in NASA/AMES wind tunnel," *International Journal of Renewable Energy Research (IJRER)*, vol. 3, pp. 261-269, 2013.
[40] B. Kim, W. Kim, S. Bae, J. Park, and M. Kim, "Aerodynamic design and performance analysis of multi-MW class wind turbine blade," *Journal of mechanical science and technology*, vol. 25, pp. 1995-2002, 2011.
[41] P. Bourdin and J. D. Wilson, "Windbreak aerodynamics: is computational fluid dynamics reliable?," *Boundary-Layer Meteorology*, vol. 126, pp. 181-208, 2008.
[42] A. ANSYS, "Version 15.0; ANSYS," *Inc.: Canonsburg, PA, USA November*, 2013.
[43] P. A. L. Gallardo, "Static and fatigue analysis of wind turbine blades subject to cold weather conditions using finite element analysis," University of Victoria, 2011.
[44] D. M. Somers, "The S825 and S826 airfoils," *National Renewable Energy Laboratory, Subcontractor Report*, 2005.
[45] R. M. Pinkerton, *Calculated and measured pressure distributions over the midspan section of the NACA 4412 airfoil* vol. 563: NACA, 1936.

[46] R. Sosa, G. Artana, E. Moreau, and G. Touchard, "Flow control with EHD actuators in middle post stall regime," *Journal of the Brazilian Society of Mechanical Sciences and Engineering*, vol. 28, pp. 200-207, 2006.
[47] O. Corning, "Production Information: Traixial Fabrics," *Toledo, Ohio*, 2003.
[48] G. W. Guideline and G. Lloyd, "Guideline for the certification of Wind Turbines," *Hamburg: Germanischer Lloyd Wind Energie Gmb H*, 2010.
[49] C. Bak, F. Zahle, R. Bitsche, T. Kim, A. Yde, L. Henriksen, *et al.*, "The DTU 10-MW reference wind turbine," *Danish wind power research*, 2013.
[50] D. T. Griffith and T. D. Ashwill, "The Sandia 100-meter all-glass baseline wind turbine blade: SNL100-00," *Sandia National Laboratories, Albuquerque, Report No. SAND2011-3779*, 2011.